

# RaCalNet: Radar Calibration Network for Sparse-Supervised Metric Depth Estimation

Xingrui Qin<sup>1</sup>, Wentao Zhao<sup>1</sup>, Chuan Cao<sup>1</sup>, Yihe Niu<sup>2</sup>, Houcheng Jiang<sup>3</sup>,  
Jingchuan Wang<sup>1\*</sup>, *Senior Member, IEEE*

**Abstract**—Dense metric depth estimation using millimeter-wave radar typically requires dense LiDAR supervision, generated via multi-frame projection and interpolation, to guide the learning of accurate depth from sparse radar measurements and RGB images. However, this paradigm is both costly and data-intensive. To address this, we propose RaCalNet, a novel framework that eliminates the need for dense supervision by using sparse LiDAR to supervise the learning of refined radar measurements, resulting in a supervision density of merely around 1% compared to dense-supervised methods. Unlike previous approaches that associate radar points with broad image regions and rely heavily on dense labels, RaCalNet first recalibrates and refines sparse radar points to construct accurate depth priors. These priors then serve as reliable anchors to guide monocular depth prediction, enabling metric-scale estimation without resorting to dense supervision. This design improves structural consistency and preserves fine details. Despite relying solely on sparse supervision, RaCalNet surpasses state-of-the-art dense-supervised methods, producing depth maps with clear object contours and fine-grained textures. Extensive experiments on the ZJU-4DRadarCam dataset and real-world deployment scenarios demonstrate its effectiveness, reducing RMSE by 35.30% and 34.89%, respectively.

## I. INTRODUCTION

Millimeter-wave (mmWave) radar provides direct metric measurements and robust performance under diverse lighting and texture variations, making it a viable sensing modality for depth completion in autonomous systems. However, mmWave point clouds are extremely sparse, often two to three orders of magnitude sparser than LiDAR, and contaminated by noise, which makes the generation of dense, high-fidelity depth maps highly challenging [1].

Current radar-guided depth estimation methods typically rely on LiDAR supervision to guide depth completion. They associate radar points with image pixels to generate semi-dense priors, which are then processed by completion networks to produce dense depth maps. Crucially, these methods rely on dense LiDAR supervision synthesized via multi-frame accumulation and interpolation. Singh [3] introduced this paradigm by aggregating 161 consecutive frames (80 past, 80 future, and the current frame) to construct dense supervision signals, a practice subsequently adopted in [2]. However, this strategy suffers from three critical limitations: (i) high data collection

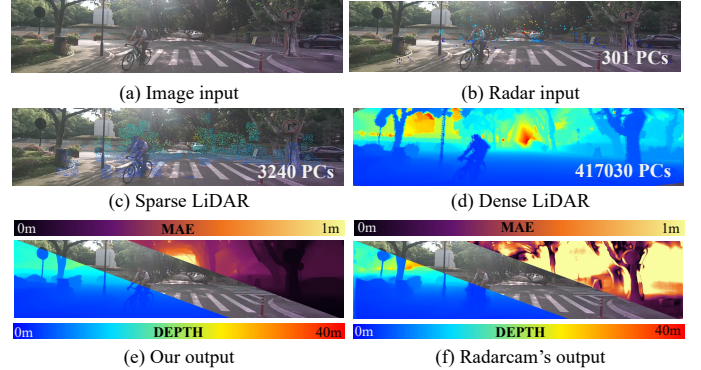


Fig. 1. Comparison of depth estimation: (a) Image input; (b) RaDAR input (projected on image); (c) sparse LiDAR supervision (3,240 points); (d) dense LiDAR supervision (417,030 points); (e) predicted depth and error map of our method using sparse laser supervision; and (f) predicted depth and error map of Radarcam [2] using dense laser supervision.

and storage costs due to the need for extensive LiDAR scans; (ii) interpolation artifacts that degrade boundary sharpness and structural accuracy; and (iii) susceptibility to dynamic scene misalignments, which introduce inconsistency and noise in the supervision signal.

To address these limitations, we propose **RaCalNet**, a novel radar-guided depth estimation framework that eliminates the need for dense LiDAR supervision by refining sparse radar points into reliable geometric anchors. Specifically, we first train a cross-modal attention module using only single-frame sparse LiDAR to learn feature correlations between radar and RGB inputs. This module predicts confidence weights for radar points, effectively suppressing noise and refining their pixel-level projections through a lightweight displacement prediction head. The resulting refined radar points are then employed as geometric anchors to calibrate monocular depth predictions via an optimization framework. By minimizing a geometric alignment loss, we solve for global scale and shift parameters that align predicted depths with radar geometry, ensuring metric consistency with physical measurements. As shown in Fig. 1, while Radarcam [2] relies on dense LiDAR supervision, our method achieves superior depth estimation using only sparse LiDAR supervision ( $\sim 1\%$  point density), yielding sharper structural boundaries and significantly reduced scale errors.

Our key contributions are summarized as follows: (i) We present a novel radar-guided depth estimation framework, RaCalNet, which eliminates the need for dense LiDAR supervision, replacing it with a recalibration and optimization

<sup>1</sup> Institute of Medical Robotics and Department of Automation, Shanghai Jiao Tong University, Shanghai, China.

<sup>2</sup> School of Mathematical Sciences, Shanghai Jiao Tong University, Shanghai, China.

<sup>3</sup> South China University of Technology, Guangzhou, China.

The first two authors contribute equal to this paper.

\* Corresponding Author: jchwang@sjtu.edu.cn.

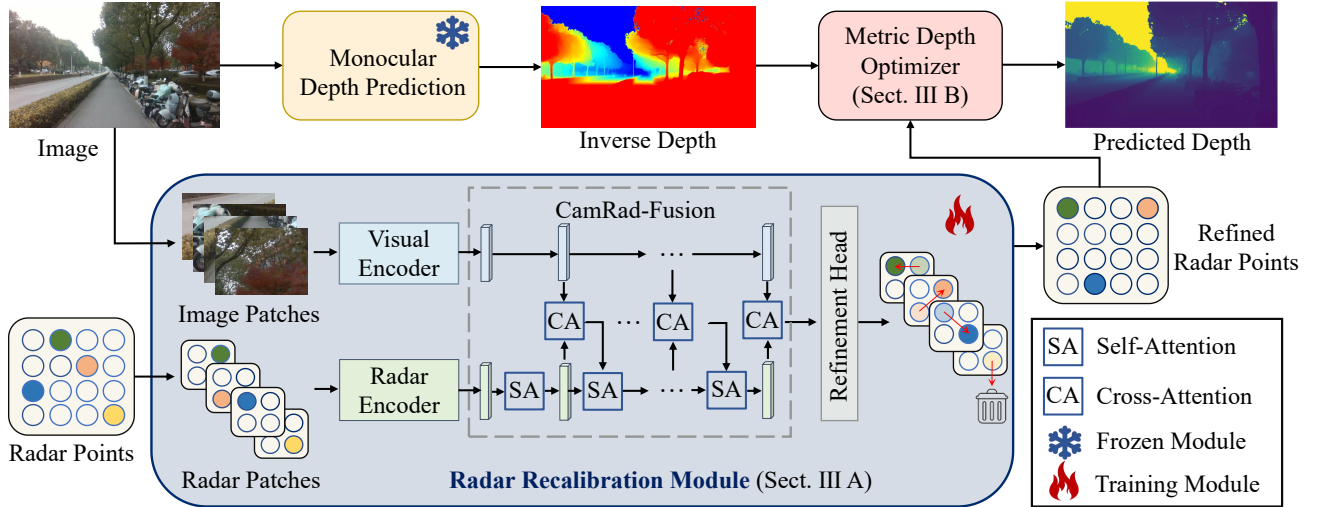


Fig. 2. Overview of our proposed RaCalNet framework. The system consists of two main components: (i) a Radar Refinement Module, which performs radar point screening and pixel-wise displacement refinement; and (ii) a Metric Depth Optimizer, which fuses refined radar with monocular depth for metric-accurate output.

strategy guided by refined radar points; (ii) we leverage a new radar refinement module with cross-modal attention to identify reliable radar points and recalibrate their pixel-level projections, generating sparse yet precise reference anchors for downstream depth prediction; (iii) We design a LiDAR-free optimization strategy that aligns monocular predictions with refined radar anchors, producing dense depth maps with accurate scale and sharp structural details; (iv) We validate our approach on the public ZJU-4DRadarCam dataset and real-world deployment scenarios, demonstrating significant performance gains over existing methods, including up to 35.30% RMSE reduction.

## II. RELATED WORK

### A. Depth Estimation with Monocular Vision

Monocular depth estimation [4]–[7] inherently suffers from scale ambiguity due to the projective nature of single-view imaging. Recent approaches employ large-scale networks [4]–[7] to produce affine-invariant depth maps that capture relative structure but lack absolute metric scale. These models benefit from extensive and diverse datasets to generalize across environments, yet typically require finetuning with external metric supervision [8]–[10] for metric alignment.

To address this, various strategies introduce auxiliary cues. VISLAM [11] performs geometric rectification of camera perspectives, while CodeVIO [9] jointly optimizes visual-inertial odometry (VIO) and dense depth through coupled estimation. Xie et al. [10] further enhance accuracy via flow-depth consistency and multi-frame triangulation. More recently, Wofk et al. [8] propose a metric depth estimation framework that globally aligns monocular predictions with sparse but accurate VIO measurements, followed by local optimization. While effective, this approach still relies on tightly coupled VIO systems and may suffer from drift or

degraded performance in textureless environments. In parallel, a series of video-based methods [12]–[16] enhance temporal consistency through learned regularization across frames. These techniques are largely orthogonal to our work and can benefit from our approach as a strong initialization stage.

While these methods significantly improve depth prediction quality, they either rely on tightly coupled VIO systems or require temporal sequences and large-scale supervision, limiting their applicability in unconstrained or dynamic environments. In contrast, our goal is to improve monocular depth accuracy by introducing sparse yet metrically accurate millimeter-wave radar as geometric anchors. Unlike VIO or dense LiDAR, radar offers robust and cost-effective metric signals that are resilient to lighting and texture variations.

### B. Depth Estimation from Radar-Camera Fusion

Fusing radar and camera data for metric depth estimation has emerged as a promising direction due to radar’s robustness to lighting and weather conditions. However, the inherent sparsity and noise of radar measurements present significant challenges for generating dense and accurate depth maps.

To address this, prior works have explored various fusion strategies. Lin et al. [17] introduced a two-stage encoder-decoder pipeline to denoise radar point clouds before fusing them with image features. Lo et al. [18] proposed height-extended radar representations to enhance spatial context. Long et al. [1] designed a Radar-to-Pixel (R2P) network that leverages Doppler velocity and optical flow to establish pixel-level correspondences between radar and image domains. Their follow-up work [19] integrated multi-sweep radar accumulation with dense LiDAR supervision in an image-guided completion framework.

Several recent methods aim to enhance fusion through confidence modeling or temporal aggregation. R4dyn [20]

treats radar points as weak supervision but focuses narrowly on dynamic vehicles. Singh et al. [3] proposed a gated fusion approach with confidence-aware radar–image correspondences, yet their method relies on accumulating up to 161 LiDAR frames for training. Radarcam [2] combines raw radar data with monocular predictions to produce dense depth maps, but also fundamentally depends on dense LiDAR supervision during training.

Despite these advances, existing methods still suffer from two key limitations: (1) they heavily rely on dense LiDAR supervision, often requiring multi-frame accumulation and interpolation; (2) they perform direct matching or regression from noisy radar points to image regions, leading to unreliable priors. In contrast, we propose to recalibrate sparse radar signals through guided refinement, enabling accurate metric-scale estimation with minimal supervision.

### III. METHOD

In this work, we address the task of dense, metrically accurate depth estimation  $\hat{d} \in \mathbb{R}_+^{H \times W}$  by fusing monocular RGB images  $I \in \mathbb{R}^{3 \times H \times W}$  with sparse radar data  $P = \{p_i \in \mathbb{R}^3\}_{i=1}^k$ . The overall architecture of our RaCalNet is illustrated in Fig. 2. Our pipeline first recalibrates and refines radar measurements using sparse LiDAR supervision in Radar Refinement Module, producing accurate depth anchors. These refined anchors are then used to optimize monocular depth predictions, specifically to correct their scale and enhance their structural consistency, resulting in accurate metric-scale estimation. Each component of our framework is detailed in the following subsections.

#### A. Radar Screening and Pixel-wise Displacement Refinement

Due to multipath reflections, sensor noise, and imperfect extrinsic calibration, the direct projection of radar points onto the image plane can result in substantial depth errors. Therefore, in addition to filtering reliable radar measurements, it is crucial to recalibrate and refine projected points within localized image regions to account for systemic errors and outliers. To achieve this, we adopt a patch-based processing strategy: for each radar point projected onto the image plane, we extract a corresponding image patch centered at its location, forming a pair of radar and image patches. These point-wise pairs are independently encoded and fused to enable fine-grained refinement.

1) Network Architecture: Unlike conventional approaches that construct a semi-dense radar depth map, our Radar recalibration module predicts both a confidence score and a pixel-wise displacement for each projected radar point. This allows the network to directly assess reliability and spatial alignment.

The radar recalibration module employs a cross-modal fusion design. The image encoder is based on ResNet-34 [21], producing hierarchical feature maps with channel dimensions of 32, 64, 128, 256, and 512. These multi-scale features are aggregated using a Feature Pyramid Network (FPN), ensuring the preservation of spatial detail and semantic richness. To

further enhance feature alignment and interaction, we incorporate channel and spatial attention mechanisms, which help highlight salient structures and suppress irrelevant background noise in a content-adaptive manner.

The radar encoder is implemented as a multi-layer perceptron (MLP) with fully connected layers of dimensions 32, 64, 128, 256, and 512. To facilitate effective radar-image fusion, image features  $\mathbf{F}_{img} \in \mathbb{R}^{B \times K \times D \times H \times W}$  are reshaped along the spatial dimensions to  $\mathbb{R}^{B \times K \times D \times N_{img}}$  with  $N_{img} = H \times W$ , so as to align with radar features  $\mathbf{F}_{rad} \in \mathbb{R}^{B \times K \times D}$ , where  $B$  is the batch size,  $K$  is the number of radar points, and  $D$  is the feature dimension. Both modalities are then flattened along the spatial axis and passed through stacked attention layers, forming the CamRad-Fusion module for effective cross-modal interaction and feature enhancement.

For each sample, radar features are represented as  $\mathbf{X}_{rad} \in \mathbb{R}^{K \times D}$ . The self-attention (SA) operation is defined as:

$$\text{SA}(\mathbf{X}_{rad}) = \text{softmax} \left( \frac{\mathbf{Q}\mathbf{K}^\top}{\sqrt{d_k}} \right) \mathbf{V}\mathbf{W}_O, \quad (1)$$

where the query, key, and value matrices are computed as  $\mathbf{Q} = \mathbf{X}_{rad}\mathbf{W}_Q$ ,  $\mathbf{K} = \mathbf{X}_{rad}\mathbf{W}_K$ , and  $\mathbf{V} = \mathbf{X}_{rad}\mathbf{W}_V$ , with learnable projections  $\mathbf{W}_Q, \mathbf{W}_K, \mathbf{W}_V \in \mathbb{R}^{D \times d_k}$  and  $\mathbf{W}_O \in \mathbb{R}^{d_k \times D}$ . This enables each radar point to attend to others and capture global contextual dependencies.

To incorporate visual context, cross-attention (CA) is applied with radar features as queries and image features as keys and values. For each radar point, the corresponding visual patch features are reshaped to  $\mathbf{X}_{img} \in \mathbb{R}^{D \times N_{img}}$  and radar features are viewed as  $\mathbf{X}_{rad} \in \mathbb{R}^{D \times 1}$ , and the attention is computed as:

$$\text{CA}(\mathbf{X}_{rad}, \mathbf{X}_{img}) = \text{softmax} \left( \frac{\mathbf{Q}\mathbf{K}^\top}{\sqrt{d_k}} \right) \mathbf{V}\mathbf{W}_O, \quad (2)$$

where  $\mathbf{Q} = \mathbf{X}_{rad}\mathbf{W}_Q$ ,  $\mathbf{K} = \mathbf{X}_{img}\mathbf{W}_K$ , and  $\mathbf{V} = \mathbf{X}_{img}\mathbf{W}_V$ . The output preserves the radar feature resolution and is reshaped back to  $\mathbb{R}^{B \times K \times D}$  for subsequent processing. This cross-modal attention allows the network to enhance radar representations with informative visual cues. Finally, the refined radar features are fed into the refinement head, which consists of a two-layer MLP that separately predicts a confidence score and a pixel-wise displacement for each radar point.

2) Confidence and Displacement Prediction: Given a radar point  $p_i$  and its corresponding image patch  $\mathcal{C}_i \in \mathbb{R}^{3 \times H \times W}$  around the projection location, RaCalNet  $h_\theta$  is designed with two output branches: a confidence prediction head  $h_\theta^{\text{conf}}$  that estimates point-wise reliability, and a displacement prediction head  $h_\theta^{\text{disp}}$  that predicts pixel-level displacement. The network outputs are defined as:

$$\hat{y}_i = h_\theta^{\text{conf}}(\mathcal{C}_i, p_i) \in [0, 1], \quad \hat{\mathbf{o}}_i = h_\theta^{\text{disp}}(\mathcal{C}_i, p_i) \in \mathbb{R}^2,$$

where  $\hat{y}_i$  represents the predicted confidence score indicating the correspondence reliability between radar point  $p_i$  and its projected pixel, while  $\hat{\mathbf{o}}_i = (\Delta u, \Delta v)$  is the estimated 2D displacement vector for refining the projected location.

With  $k$  radar points in the cloud  $P$ , these predictions guide the reliability screening and spatial refinement process:

$$(u_i^{\text{ref}}, v_i^{\text{ref}}) = \begin{cases} (u_i, v_i) + \hat{\mathbf{o}}_i, & \text{if } \hat{y}_i \geq \tau \\ \text{discarded}, & \text{otherwise} \end{cases} \quad (3)$$

Here,  $(u_i, v_i)$  is the original 2D projection of radar point  $p_i$ , and  $\hat{\mathbf{o}}_i = (\Delta u, \Delta v)$  is the predicted displacement. The refined coordinate  $(u_i^{\text{ref}}, v_i^{\text{ref}})$  is used only if the predicted confidence  $\hat{y}_i$  exceeds a predefined threshold  $\tau$ ; otherwise, the point is discarded.

3) Training: The network is trained using sparse LiDAR points projected onto the image plane as depth ground truth, denoted as  $d_{gt}(x, y)$  for valid LiDAR pixel locations. Dual learning objectives are defined over the radar points  $p \in P$  for confidence classification and displacement regression.

*Confidence Labels and Loss:* For each radar point  $p$  with projected pixel location  $(u_p, v_p)$ , we define a local neighborhood  $\mathcal{R}(p)$  (e.g.,  $5 \times 5$  pixels). The binary confidence label  $y_p^{(conf)} \in \{0, 1\}$  is assigned based on the count of valid LiDAR points within  $\mathcal{R}(p)$  that meet the depth consistency criterion:

$$y_p^{(conf)} = \begin{cases} 1 & \text{if } |\{x \in \mathcal{R}(p) \mid d_{gt}(x) > 0 \\ & \text{and } |d_{gt}(x) - d(p)| < \tau(p)\}| \geq \eta \\ 0 & \text{otherwise} \end{cases} \quad (4)$$

where  $\eta$  is a minimum count threshold (e.g.,  $\eta = 3$ ), and the adaptive depth error threshold  $\tau(p)$  is defined based on the radar point's measured range  $d(p)$ :

$$\tau(p) = \begin{cases} 0.5 \text{ m} & d(p) < 30 \text{ m} \\ 0.75 \text{ m} & 30 \text{ m} \leq d(p) \leq 50 \text{ m} \\ 1.0 \text{ m} & d(p) > 50 \text{ m} \end{cases} \quad (5)$$

The confidence classification loss is the binary cross-entropy over all radar points with valid LiDAR ground truth available in their neighborhood:

$$\mathcal{L}_{conf} = \frac{1}{|P_{valid}|} \sum_{p \in P_{valid}} \left[ y_p^{(conf)} \log \hat{y}_p^{(conf)} + (1 - y_p^{(conf)}) \log(1 - \hat{y}_p^{(conf)}) \right] \quad (6)$$

Here,  $\hat{y}_p^{(conf)} = h_{\theta}^{\text{conf}}(\mathcal{C}_i, p)$  is the predicted confidence, and  $P_{valid} = \{p \in P \mid \exists x \in \mathcal{R}(p), d_{gt}(x) > 0\}$  is the set of radar points where LiDAR ground truth exists within their defined local neighborhood for label assignment.

*Displacement Labels and Loss:* For each radar point  $p$ , we search within a larger local  $h \times w$  neighborhood  $\mathcal{N}(p)$  centered on its projection  $(u_p, v_p)$ . A smaller sliding window of size  $h^* \times w^*$  is convolved over  $\mathcal{N}(p)$ . The displacement label  $y_p^{(disp)}$  is determined by the offset from  $(u_p, v_p)$  to the center of the window position  $\mathbf{c}^*$  that contains the maximum number of valid LiDAR points satisfying the depth consistency criterion:

$$\mathbf{c}^* = \arg \max_{\mathbf{c} \in \mathcal{N}(p)} \left\{ \begin{aligned} &|x \in \mathcal{W}_c \mid d_{gt}(x) > 0 \\ &\text{and } |d_{gt}(x) - d(p)| < \tau(p) \end{aligned} \right\} \quad (7)$$

$$y_p^{(disp)} = \mathbf{c}^* - (u_p, v_p) \quad (8)$$

where  $\mathcal{W}_c$  denotes the set of pixels within the sliding window centered at candidate location  $\mathbf{c}$ . The predicted pixel displacement  $\hat{y}_p^{(disp)}$  is supervised using the Smooth L1 loss:

$$\mathcal{L}_{disp} = \frac{1}{|P_{valid}|} \sum_{p \in P_{valid}} \text{SmoothL1}(\hat{y}_p^{(disp)}, y_p^{(disp)}) \quad (9)$$

Here,  $\hat{y}_p^{(disp)} = h_{\theta}^{\text{disp}}(\mathcal{C}_i, p)$ . The final training loss combines both objectives:

$$\mathcal{L}_{total} = \lambda_{conf} \mathcal{L}_{conf} + \lambda_{disp} \mathcal{L}_{disp} \quad (10)$$

## B. Metric Depth Optimization

We now recover the final metrically scaled depth map by aligning the scale-ambiguous monocular inverse depth predictions with radar-based metric measurements. A frozen monocular depth estimation network [22] is employed to generate dense, scale-ambiguous inverse depth maps  $\hat{d}_m \in \mathbb{R}_+^{H \times W}$ . This transformer-based model [23], trained using scale-invariant losses over diverse datasets, preserves fine-grained textures and sharp geometric boundaries, which are essential for downstream metric refinement.

Let  $d_{\text{radar}}^{(i)}$  denote the refined metric depth of radar point  $p_i$ , and  $(u_i, v_i)$  its corresponding image coordinates. To align these measurements with the predicted  $\hat{d}_m$ , we solve the following least squares problem to find optimal scale  $\alpha$  and shift  $\beta$ :

$$\min_{\alpha, \beta} \sum_{i \in \mathcal{S}} \left( \frac{1}{d_{\text{radar}}^{(i)}} - \alpha \cdot \hat{d}_m(u_i, v_i) - \beta \right)^2 \quad (11)$$

where  $\mathcal{S}$  denotes the subset of radar points used for alignment. To ensure robustness, we discard outliers by filtering invalid or unreliable regions in  $\hat{d}_m$ .

Instead of using a fixed threshold, we adopt a dynamic threshold selection strategy. Specifically, we define a candidate set of inverse depth thresholds  $\mathcal{T}_d = \{t_1, t_2, \dots, t_M\}$ , and determine the best threshold  $T^*$  by selecting the one that yields the lowest fitting error. For each threshold  $t \in \mathcal{T}_d$ , we define the corresponding valid set:

$$\mathcal{S}_t = \left\{ i \mid 0 < \hat{d}_m(u_i, v_i) < t \right\} \quad (12)$$

and compute its associated parameters  $(\alpha_t, \beta_t)$  using Equation (11). The optimal threshold  $T^*$  and corresponding parameters are selected as:

$$T^* = \arg \min_{t \in \mathcal{T}_d} \sum_{i \in \mathcal{S}_t} \left( \frac{1}{d_{\text{radar}}^{(i)}} - \alpha_t \cdot \hat{d}_m(u_i, v_i) - \beta_t \right)^2 \quad (13)$$

Finally, the recovered metric depth map  $\hat{d}$  is obtained by inverting the affine-aligned inverse depth:

$$\hat{d}(u, v) = \begin{cases} \frac{1}{\alpha^* \cdot \hat{d}_m(u, v) + \beta^*} & \text{if } \hat{d}_m(u, v) \neq 0 \\ \text{undefined} & \text{otherwise} \end{cases} \quad (14)$$

---

**Algorithm 1** Global Metric Depth Optimization
 

---

**Require:** Monocular inverse depth map  $\hat{d}_m$ , radar points  $\{(u_i, v_i, d_{\text{radar}}^{(i)})\}_{i=1}^N$ , threshold set  $\mathcal{T}_d$

**Ensure:** Optimized depth map  $\hat{d}$

- 1: Initialize  $L^* \leftarrow +\infty, T^* \leftarrow 0$
- 2: **for all**  $t \in \mathcal{T}_d$  **do**
- 3:  $\mathcal{S}_t \leftarrow \{i \mid 0 < \hat{d}_m(u_i, v_i) < t\}$
- 4: Fit  $(\alpha_t, \beta_t)$  by minimizing:

$$\sum_{i \in \mathcal{S}_t} \left( \frac{1}{d_{\text{radar}}^{(i)}} - \alpha \cdot \hat{d}_m(u_i, v_i) - \beta \right)^2$$

- 5: Compute  $L_t$
  - 6: **if**  $L_t < L^*$  **then**
  - 7:  $L^* \leftarrow L_t, T^* \leftarrow t, (\alpha^*, \beta^*) \leftarrow (\alpha_t, \beta_t)$
  - 8: **end if**
  - 9: **end for**
  - 10: **for all**  $(u, v)$  such that  $\hat{d}_m(u, v) \neq 0$  **do**
  - 11:  $\hat{d}(u, v) \leftarrow \frac{1}{\alpha^* \cdot \hat{d}_m(u, v) + \beta^*}$
  - 12: **end for**
  - 13: **return**  $\hat{d}$
- 

Note that Equation (14) leaves regions with zero inverse depth undefined, which typically correspond to sky or invalid areas. This design enables flexible handling for downstream applications, where such regions can be explicitly filled using task-specific strategies (e.g., assigning 0 or a large constant). To summarize the process, the optimization pipeline is outlined in Algorithm 1.

## IV. EXPERIMENTS

### A. Datasets

1) ZJU-4DRadarCam Dataset [2]: We first evaluate our method on this public dataset, which was collected using a ground robotic platform equipped with an Oculii’s EAGLE 4D radar, a RealSense D455 camera, and a RoboSense M1 LiDAR sensor. It primarily covers diverse driving scenarios in both urban and off-road environments. The dataset contains 33,409 synchronized radar-camera keyframes, with 29,312 frames designated for training and validation, and 4,097 frames reserved for testing.

2) Real-World Deployment Scenarios: To further validate the generalizability of our approach beyond public datasets, we collected our own proprietary multimodal data in real-world deployment scenarios. These were captured using a ground robotic platform equipped with a ZF FRGen21 4D radar, a RealSense D435I camera, and a Livox HAP LiDAR which served as the source of ground truth depth labels (see Fig. 3). The data was collected primarily in campus environments and consists of 22,423 synchronized radar-camera keyframes, with 20,156 used for training and validation and 2,267 reserved for testing.

### B. Training Details and Evaluation Protocol

For the ZJU-4DRadarCam dataset, we addressed alignment inaccuracies stemming from imperfect sensor calibration (il-

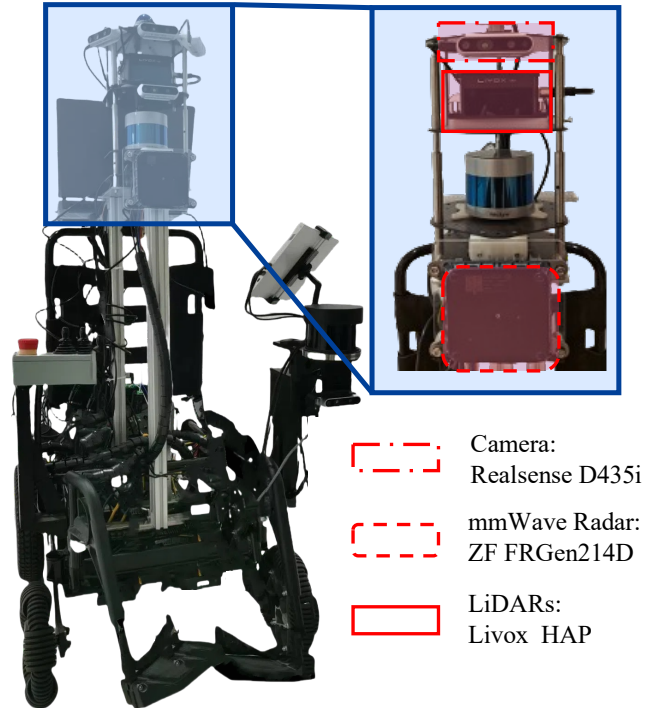


Fig. 3. Data collection platform and sensors. (Left) Overall view of the ground robotic platform used for real-world data collection. (Right) Close-up views of the multimodal sensors: RealSense D435I camera (top), Livox HAP LiDAR (middle), and ZF FRGen21 4D radar (bottom).

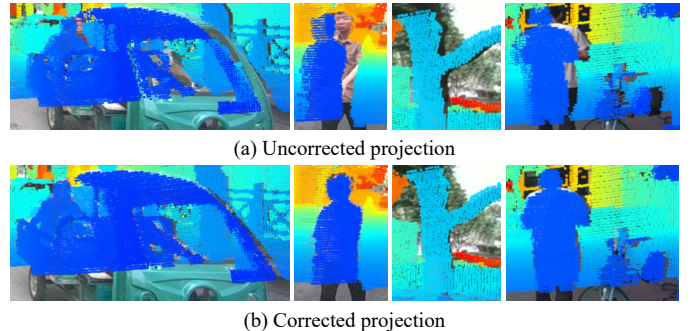


Fig. 4. Visualization of depth inaccuracies in the ZJU-4DRadarCam dataset. The top row illustrates misalignment in the LiDAR depth map (the original ground truth), primarily caused by calibration errors. The bottom row shows our recalibrated version of the ground truth, where the depth projection exhibits significantly improved accuracy.

lustrated in Fig. 4) by optimizing extrinsic parameters and reprojecting the original LiDAR points. This recalibration process significantly improved geometric consistency between LiDAR measurements and RGB images. Throughout our experiments, our method exclusively employs sparse single-frame LiDAR supervision, while comparative methods maintain their original configurations using multi-frame projected and interpolated dense LiDAR for training. To validate methodological robustness in real-world deployment scenarios, we maintained identical supervision protocols: our approach utilized sparse single-frame LiDAR supervision, whereas all baselines em-

TABLE I  
EVALUATIONS ON ZJU-4DRADARCAM (MM)

Dist	Method	MAE↓	RMSE↓	AbsRel↓	SqRel↓	$\delta_1 \uparrow$
50m	Radarcam [2]	1468.645	3408.806	0.116	848.655	0.879
	Ours	<b>1212.372</b>	<b>2137.652</b>	<b>0.095</b>	<b>535.929</b>	<b>0.895</b>
70m	Radarcam [2]	1572.917	3719.426	0.117	875.905	0.877
	Ours	<b>1317.045</b>	<b>2358.958</b>	<b>0.097</b>	<b>572.155</b>	<b>0.893</b>
80m	Radarcam [2]	1603.922	3831.740	0.117	886.439	0.877
	Ours	<b>1343.483</b>	<b>2479.008</b>	<b>0.098</b>	<b>583.625</b>	<b>0.892</b>

ployed their native training configurations relying on multi-frame densified LiDAR supervision.

The encoder backbone was initialized with ImageNet pre-trained weights [24], while all other layers were randomly initialized. For the ZJU-4DRadarCam dataset, input images were resized and cropped to  $352 \times 640$ , with a fixed region-of-interest (ROI) size of  $35 \times 35$ . We employed the Adam optimizer ( $\beta_1=0.9$ ,  $\beta_2=0.999$ ) with an initial learning rate of  $2 \times 10^{-4}$ , decayed step-wise over 130 epochs to a final rate of  $1 \times 10^{-6}$ . The same data augmentation strategies were applied to both datasets: random horizontal flipping (probability = 0.5), and random variations in saturation, brightness, and contrast.

For real-world deployment scenarios, input images were resized to  $224 \times 416$  while maintaining the same ROI configuration. The optimizer and hyperparameter settings remained identical, except for a longer training schedule of 150 epochs. All models were trained on an NVIDIA RTX 3090 GPU with a batch size of 28, and the full training process for RaCalNet took approximately 24 hours.

For quantitative evaluation of depth estimation performance, we adopt standard metrics widely used in prior work [25], including Mean Absolute Error (MAE), Root Mean Square Error (RMSE), Absolute Relative Error (AbsRel), Squared Relative Error (SqRel), and thresholded accuracy ( $\delta_1$ ).

### C. Evaluation on ZJU-4DRadarCam

We conducted a comprehensive evaluation of dense depth estimation performance across 50m, 70m, and 80m ranges. As reported in Table I, our RaCalNet framework consistently achieves state-of-the-art performance across all evaluated ranges, significantly outperforming the prior SOTA approach [2] using their best-performing configuration (DPT+Var+RC-Net). Specifically, RaCalNet achieves RMSE reductions of 35.08%, 29.12%, and 27.27% at 50m, 70m, and 80m ranges respectively. These improvements stem from our two-stage architecture: first identifying reliable radar points and refining pixel-level projections, followed by global optimization that aligns monocular predictions to metric scale while preserving structural integrity.

Fig. 5 presents visual comparisons organized in five rows: (1) input image, (2) depth map predicted by Radarcam [2], (3) depth map predicted by our RaCalNet, (4) error map of Radarcam, and (5) error map of RaCalNet (all in meters). Red boxes highlight regions where RaCalNet exhibits noticeably better performance. The results show that our method accurately segments sky regions, delineates object boundaries with

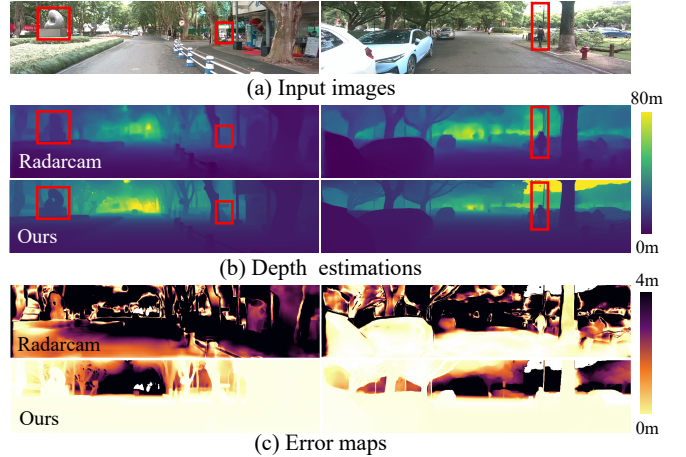


Fig. 5. Experimental results for ZJU-4DRadarCam (from top to bottom): (a) Input image, (b) Radarcam’s [2] and our RaCalNet depth estimations, (c) Radarcam’s and our errors. All values are in meters (m). Red boxes highlight superior performance regions.

TABLE II  
EVALUATIONS ON REAL-WORLD DEPLOYMENT (MM)

Dist	Method	MAE↓	RMSE↓	AbsRel↓	SqRel↓	$\delta_1 \uparrow$
50m	Radarcam [2]	1469.553	3237.304	0.112	660.747	0.884
	Ours	<b>1272.727</b>	<b>1982.943</b>	<b>0.091</b>	<b>376.293</b>	<b>0.905</b>
70m	Radarcam [2]	1674.472	3681.323	0.113	707.069	0.882
	Ours	<b>1391.237</b>	<b>2340.489</b>	<b>0.094</b>	<b>425.510</b>	<b>0.899</b>
80m	Radarcam [2]	1721.122	3875.754	0.114	729.197	0.881
	Ours	<b>1475.972</b>	<b>2523.246</b>	<b>0.096</b>	<b>446.519</b>	<b>0.897</b>

high precision, and effectively suppresses artifacts in complex scenes.

### D. Evaluation on Real-World Deployment Scenarios

Following the same evaluation protocol as in Section IV-C, we further validate the proposed framework using proprietary real-world deployment data. As summarized in Table II, our method consistently outperforms existing radar-guided depth estimation baselines [2] across all tested distance ranges.

In particular, compared to [2], our method achieves substantial RMSE reductions of 46.24%, 43.42%, and 40.06% at 50m, 70m, and 80m intervals, respectively. These results set a new benchmark for long-range radar-based dense depth completion.

Qualitative comparisons in Fig. 6 further illustrate the improvements in visual consistency, depth boundary clarity, and artifact suppression achieved by our method, particularly in challenging outdoor scenarios.

### E. Ablation Study

We conduct detailed ablation studies on the real-world deployment data to analyze the contribution of individual components in our framework. Specifically, we evaluate three configurations: (1) the complete RaCalNet pipeline; (2) a

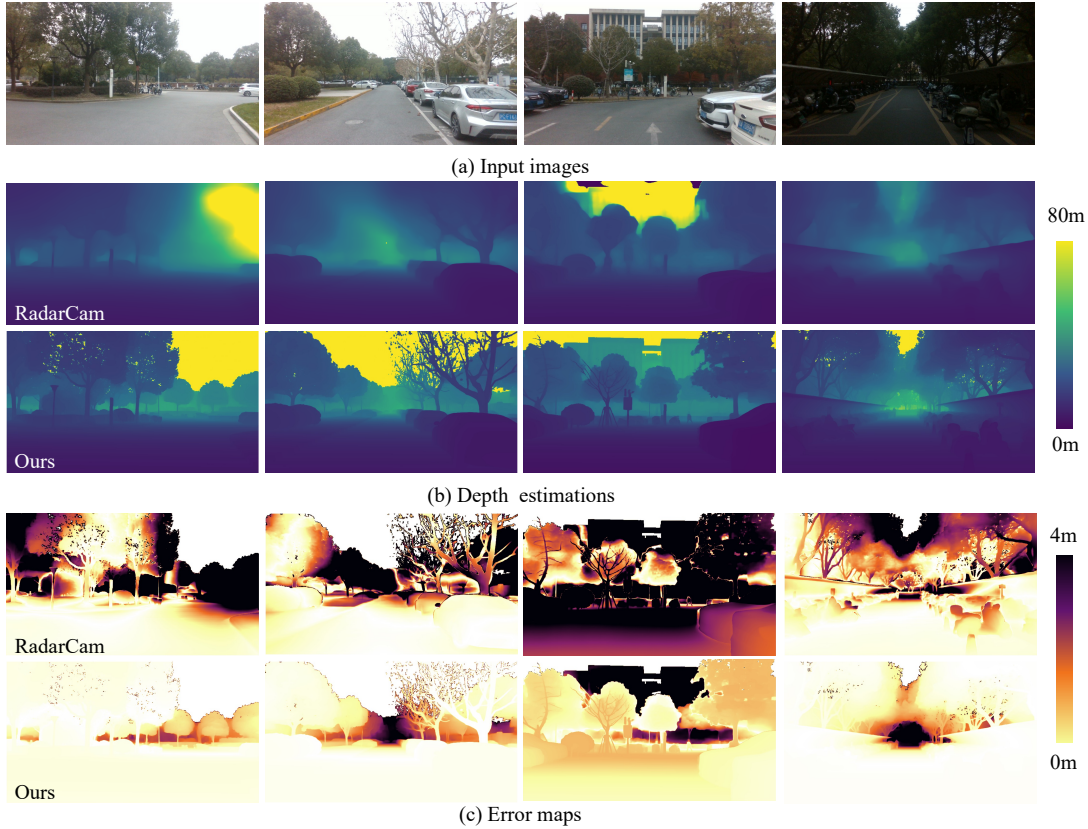


Fig. 6. Experimental results for proprietary real-world data (from top to bottom): (a) Input image, (b) RadarCam’s [2] and our RaCalNet depth estimations, (c) RadarCam’s [2] and our errors. All values are in meters (m).

TABLE III  
ABLATION OF OUR MODULE (MM)

Dist	Configuration	MAE↓	RMSE↓	AbsRel↓	SqRel↓	$\delta_1$ ↑
50m	Complete RaCalNet	<b>1272.727</b>	<b>1982.943</b>	<b>0.091</b>	<b>376.293</b>	<b>0.905</b>
	w/o Displacement Refinement	1326.122	2055.036	0.095	389.973	0.901
	w/o Radar Refinement	2505.368	3487.922	0.179	543.408	0.802
70m	Complete RaCalNet	<b>1391.237</b>	<b>2340.489</b>	<b>0.094</b>	<b>425.510</b>	<b>0.899</b>
	w/o Displacement Refinement	1476.192	2439.610	0.099	443.531	0.894
	w/o Radar Refinement	2774.884	4227.314	0.182	644.136	0.787
80m	Complete RaCalNet	<b>1475.972</b>	<b>2523.246</b>	<b>0.096</b>	<b>446.519</b>	<b>0.897</b>
	w/o Displacement Refinement	1572.627	2608.443	0.102	461.596	0.892
	w/o Radar Refinement	2833.835	4470.089	0.184	675.578	0.785

variant retaining radar screening but without Pixel-wise Displacement Refinement; and (3) a variant excluding the entire Radar Refinement Module (both screening and displacement refinement). Results are shown in Table III and reveal the following insights:

1) Displacement Refinement Ablation: When retaining radar screening but disabling the pixel-level displacement refinement, we observe consistent performance drops (4.0-6.1% MAE increase across all ranges). This reveals two key insights: (i) even screened radar points require sub-pixel alignment adjustments due to residual calibration errors and temporal synchronization issues, and (ii) the learned displacement refinement effectively compensates for these imperfections while preserving the geometric validity of radar projections. The improvement is particularly notable at longer distances (70-

80m) where calibration errors have more pronounced effects.

2) Impact of Radar Refinement: The complete removal of the Radar Refinement Module (both screening and displacement components) leads to severe performance degradation, with MAE increasing by 96.8% at 50m (2505mm vs. 1273mm) and 92.1% at 80m (2834mm vs. 1476mm). This demonstrates that raw radar measurements contain substantial noise and calibration errors that directly propagate to depth predictions. Our refinement module is crucial for: (i) identifying reliable radar points through cross-modal screening, and (ii) establishing accurate pixel-level correspondences, both being essential for maintaining metric accuracy in the fused output.

#### F. Impact on Downstream Tasks: 3D Scene Reconstruction

To demonstrate the practical benefits of high-quality depth estimation, we evaluate the influence of different depth prediction methods on a downstream 3D scene reconstruction task. Specifically, we employ FrozenRecon [26], a 3D reconstruction framework that takes as input RGB images, depth maps, camera intrinsics, and optionally camera poses to produce dense 3D scene representations.

In our experiment, we supply the same RGB images and ground-truth camera intrinsics across all methods to ensure fair comparison. Camera poses are left to be optimized by FrozenRecon during reconstruction. The only varying input is the predicted depth map, which is either produced by prior

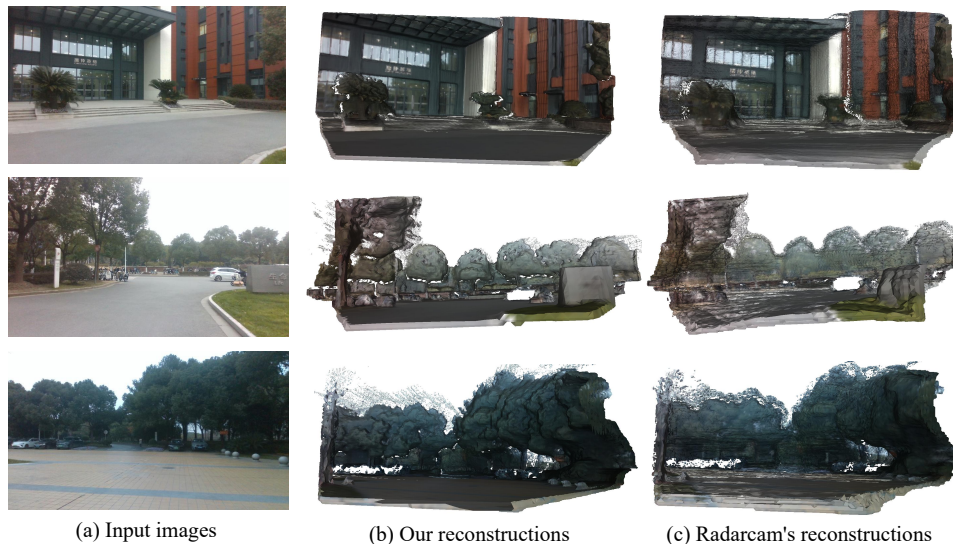


Fig. 7. Qualitative comparison of 3D scene reconstruction results. (a) Input monocular RGB images. (b) Reconstructions based on depth estimated by our method. (c) Reconstructions using depth predicted by Radarcam. Our approach yields more complete and geometrically accurate results.

radar-guided depth estimation methods or by our full method integrating RaCalNet and the global optimization module.

Fig. 7 shows qualitative comparisons of the reconstructed 3D scenes. Depth predictions from our method lead to noticeably more complete and geometrically accurate reconstructions, particularly in ground regions and structurally complex areas. These improvements underscore the broader utility of our framework, extending its value beyond standalone depth estimation to general 3D perception tasks.

## V. CONCLUSIONS

We propose RaCalNet, a novel framework for dense metric depth estimation using radar and monocular images, which eliminates the need for dense LiDAR supervision. Instead, it leverages sparse LiDAR to supervise the refinement of raw radar points, generating accurate, pixel-wise depth anchors. These anchors are then used to calibrate scale and optimize monocular depth predictions, addressing key challenges such as radar unreliability and the distortion introduced by dense LiDAR interpolation.

Extensive experiments on public benchmarks and real-world scenarios demonstrate that RaCalNet significantly outperforms prior radar-guided methods, despite relying on only  $\sim 1\%$  of the supervision density used in dense LiDAR-based approaches. The resulting depth maps preserve structural details and support downstream tasks such as 3D reconstruction. Our work introduces a new paradigm for radar-guided monocular depth estimation, providing a promising foundation for future research. In the future, we plan to explore temporal modeling across sequential frames to further improve robustness and accuracy.

## REFERENCES

- [1] Y. Long, D. Morris, X. Liu, M. Castro, P. Chakravarthy, and P. Narayanan, "Full-velocity radar returns by radar-camera fusion," in *Proceedings of the IEEE/CVF International Conference on Computer Vision*, 2021, pp. 16 198–16 207.
- [2] H. Li, Y. Ma, Y. Gu, K. Hu, Y. Liu, and X. Zuo, "Radarcam-depth: Radar-camera fusion for depth estimation with learned metric scale," in *2024 IEEE International Conference on Robotics and Automation (ICRA)*. IEEE, 2024, pp. 10 665–10 672.
- [3] A. D. Singh, Y. Ba, A. Sarker, H. Zhang, A. Kadambi, S. Soatto, M. Srivastava, and A. Wong, "Depth estimation from camera image and mmwave radar point cloud," in *Proceedings of the IEEE/CVF Conference on Computer Vision and Pattern Recognition*, 2023, pp. 9275–9285.
- [4] R. Birkl, D. Wofk, and M. Müller, "Midas v3. 1—a model zoo for robust monocular relative depth estimation," *arXiv preprint arXiv:2307.14460*, 2023.
- [5] W. Yin, J. Zhang, O. Wang, S. Niklaus, L. Mai, S. Chen, and C. Shen, "Learning to recover 3d scene shape from a single image," in *Proceedings of the IEEE/CVF Conference on Computer Vision and Pattern Recognition*, 2021, pp. 204–213.
- [6] R. Ranftl, A. Bochkovskiy, and V. Koltun, "Vision transformers for dense prediction," in *Proceedings of the IEEE/CVF international conference on computer vision*, 2021, pp. 12 179–12 188.
- [7] L. Yang, B. Kang, Z. Huang, X. Xu, J. Feng, and H. Zhao, "Depth anything: Unleashing the power of large-scale unlabeled data," in *Proceedings of the IEEE/CVF Conference on Computer Vision and Pattern Recognition*, 2024, pp. 10 371–10 381.
- [8] D. Wofk, R. Ranftl, M. Müller, and V. Koltun, "Monocular visual-inertial depth estimation," in *2023 IEEE International Conference on Robotics and Automation (ICRA)*. IEEE, 2023, pp. 6095–6101.
- [9] X. Zuo, N. Merrill, W. Li, Y. Liu, M. Pollefeys, and G. Huang, "Codevio: Visual-inertial odometry with learned optimizable dense depth," in *2021 IEEE international conference on robotics and automation (icra)*. IEEE, 2021, pp. 14 382–14 388.
- [10] J. Xie, C. Lei, Z. Li, L. E. Li, and Q. Chen, "Video depth estimation by fusing flow-to-depth proposals," in *2020 IEEE/RSJ International Conference on Intelligent Robots and Systems (IROS)*. IEEE, 2020, pp. 10 100–10 107.
- [11] K. Sartipi, T. Do, T. Ke, K. Vuong, and S. I. Roumeliotis, "Deep depth estimation from visual-inertial slam," in *2020 IEEE/RSJ International Conference on Intelligent Robots and Systems (IROS)*. IEEE, 2020, pp. 10 038–10 045.
- [12] J. Kopf, X. Rong, and J.-B. Huang, "Robust consistent video depth estimation," in *Proceedings of the IEEE/CVF Conference on Computer Vision and Pattern Recognition*, 2021, pp. 1611–1621.

- [13] Y.-C. Lee, K.-W. Tseng, G.-S. Chen, and C.-S. Chen, "Globally consistent video depth and pose estimation with efficient test-time training," *arXiv preprint arXiv:2208.02709*, 2022.
- [14] W. Zhao, Y. Niu, Y. Wang, T. Deng, S. Yuan, Z. Wang, R. Guo, and J. Wang, "Uno: Unified self-supervised monocular odometry for platform-agnostic deployment," 2025. [Online]. Available: <https://arxiv.org/abs/2506.07013>
- [15] T. Deng, Y. Wang, H. Xie, H. Wang, R. Guo, J. Wang, D. Wang, and W. Chen, "Neslam: Neural implicit mapping and self-supervised feature tracking with depth completion and denoising," *IEEE Transactions on Automation Science and Engineering*, 2025.
- [16] W. Zhao, Y. Wang, Z. Wang, R. Li, P. Xiao, J. Wang, and R. Guo, "Self-supervised deep monocular visual odometry and depth estimation with observation variation," *Displays*, vol. 80, p. 102553, 2023.
- [17] J.-T. Lin, D. Dai, and L. Van Gool, "Depth estimation from monocular images and sparse radar data," in *2020 IEEE/RSJ International Conference on Intelligent Robots and Systems (IROS)*. IEEE, 2020, pp. 10 233–10 240.
- [18] C.-C. Lo and P. Vandewalle, "Depth estimation from monocular images and sparse radar using deep ordinal regression network," in *2021 IEEE International Conference on Image Processing (ICIP)*. IEEE, 2021, pp. 3343–3347.
- [19] Y. Long, D. Morris, X. Liu, M. Castro, P. Chakravarty, and P. Narayanan, "Radar-camera pixel depth association for depth completion," in *Proceedings of the IEEE/CVF Conference on Computer Vision and Pattern Recognition*, 2021, pp. 12 507–12 516.
- [20] S. Gasperini, P. Koch, V. Dalletta, N. Navab, B. Busam, and F. Tombari, "R4dyn: Exploring radar for self-supervised monocular depth estimation of dynamic scenes," in *2021 International Conference on 3D Vision (3DV)*. IEEE, 2021, pp. 751–760.
- [21] K. He, X. Zhang, S. Ren, and J. Sun, "Deep residual learning for image recognition," in *Proceedings of the IEEE conference on computer vision and pattern recognition*, 2016, pp. 770–778.
- [22] S. Chen, H. Guo, S. Zhu, F. Zhang, Z. Huang, J. Feng, and B. Kang, "Video depth anything: Consistent depth estimation for super-long videos," *arXiv preprint arXiv:2501.12375*, 2025.
- [23] A. Dosovitskiy, L. Beyer, A. Kolesnikov, D. Weissenborn, X. Zhai, T. Unterthiner, M. Dehghani, M. Minderer, G. Heigold, S. Gelly *et al.*, "An image is worth 16x16 words: Transformers for image recognition at scale," *arXiv preprint arXiv:2010.11929*, 2020.
- [24] J. Deng, W. Dong, R. Socher, L.-J. Li, K. Li, and L. Fei-Fei, "Imagenet: A large-scale hierarchical image database," in *2009 IEEE conference on computer vision and pattern recognition*. Ieee, 2009, pp. 248–255.
- [25] J. Sun, Y. Xie, L. Chen, X. Zhou, and H. Bao, "Neuralrecon: Real-time coherent 3d reconstruction from monocular video," in *Proceedings of the IEEE/CVF conference on computer vision and pattern recognition*, 2021, pp. 15 598–15 607.
- [26] G. Xu, W. Yin, H. Chen, C. Shen, K. Cheng, and F. Zhao, "Frozen-recon: Pose-free 3d scene reconstruction with frozen depth models," in *2023 IEEE/CVF International Conference on Computer Vision (ICCV)*. IEEE, 2023, pp. 9276–9286.